PHYSICS

Highly mobile charge-transfer excitons in two-dimensional WS_2/tetracene heterostructures

Tong Zhu,* Long Yuan,* Yan Zhao, Mingwei Zhou, Yan Wan, Jianguo Mei, Libai Huang†

Charge-transfer (CT) excitons at heterointerfaces play a critical role in light to electricity conversion using organic and nanostructured materials. However, how CT excitons migrate at these interfaces is poorly understood. We investigate the formation and transport of CT excitons in two-dimensional WS_2/tetracene van der Waals heterostructures. Electron and hole transfer occurs on the time scale of a few picoseconds, and emission of interlayer CT excitons with a binding energy of ~0.3 eV has been observed. Transport of the CT excitons is directly measured by transient absorption microscopy, revealing coexistence of delocalized and localized states. Trapping-detrapping dynamics between the delocalized and localized states leads to stretched-exponential photoluminescence decay with an average lifetime of ~2 ns. The delocalized CT excitons are remarkably mobile with a diffusion constant of ~1 $cm^2 s^{-1}$. These highly mobile CT excitons could have important implications in achieving efficient charge separation.

INTRODUCTION

Charge transfer and separation at heterointerfaces play a key role in determining the efficiency of light to electricity conversion using organic and nanostructured materials (*1*–*5*). In these systems, charge separation occurs when an exciton created in one material is dissociated into a spatially separated electron-hole (e-h) pair across the interface. Semiconducting transition metal dichalcogenides (TMDCs) are versatile building blocks for fabricating two-dimensional (2D) van der Waals (vdW) heterostructures with atomically thin and sharp interfaces, allowing for applications such as photovoltaics and photodetectors (*6*–*10*). Molecular and polymeric semiconductors can also be integrated with 2D TMDCs to form vdW heterostructures (*11*–*15*), and charge generation at organic-TMDC interfaces has been recently demonstrated (*14*).

Charge transfer at the interface of TMDC heterostructures has been found to be extremely rapid, as short as 50 fs (*15*–*19*). However, because of the inefficient screening of the interfacial Coulomb potential, the spatially separated e-h pair are not free but bound with energy on the order of hundreds of millielectron volts (*20*), leading to the formation of charge-transfer (CT) excitons also known as interlayer excitons in TMDC heterostructures (such as MoS_2/WS_2) (*16*–*18*, *21*–*24*). When incorporated with molecular semiconductors, the nature of the interfacial CT states following CT events remains elusive at the 2D organic-TMDC interfaces. Although CT excitons have been inferred in recent studies (*14*, *15*), no direct experimental evidence has been provided.

CT exciton diffusion has been proposed as a mechanism for the electrons and holes to escape the large interfacial Coulomb potential to achieve charge separation (*25*). However, the CT states so far have been mostly studied in largely disordered systems such as organic solar cells (*1*–*3*, *25*–*27*), where measurements are averaged over many different kinds of interfaces making it difficult to obtain the upper limit of CT exciton transport. To overcome this difficulty, we use heterostructures that integrate exfoliated WS_2 layers with tetracene thin films as a model system with 2D crystalline organic-inorganic interfaces. Another challenge is that direct measurements of CT exciton transport require quantitative information in both spatial and temporal domains. Recent photoluminescence (PL) microscopy measurements have revealed that CT excitons move 5 to 10 nm in space at disordered organic-organic interfaces (*25*). However, a drawback for PL-based techniques is that only emissive species are investigated, whereas many of the CT states are nonemissive. To address this challenge, we use transient absorption microscopy (TAM) that is capable of imaging both emissive and nonemissive excitons with ~200 fs temporal resolution and ~50-nm spatial precision (*28*). The measurements on WS_2/Tc heterostructures presented here reveal highly mobile CT excitons with a diffusion constant of ~1 $cm^2 s^{-1}$, which could be an important factor in achieving efficient charge separation at 2D organic-TMDC interfaces.

RESULTS AND DISCUSSION

CT excitons emission and dynamics

Figure 1 shows the construction of a heterostructure from a single-layer WS_2 (1L-WS_2) and a tetracene (Tc) thin film. The optical image of the exfoliated 1L-WS_2 flake before the Tc deposition is shown in Fig. 1A, and the reflection spectrum is shown in fig. S1. Polycrystalline Tc thin film is deposited onto the WS_2 flakes by physical vapor deposition, as detailed in the Supplementary Materials. A film thickness of ~20 nm is determined using atomic force microscopy (AFM) (Fig. 1B and fig. S2). The Tc molecules are likely to pack edge-on in the herringbone structure on WS_2, as schematically shown in Fig. 1C (*29*).

Figure 1D compares the steady-state PL spectra from the 1L-WS_2/Tc heterostructure, a Tc-only region of the film, and the 1L-WS_2 before deposition of Tc, with photoexcitation at 2.8 eV exciting both the 1L-WS_2 and the Tc film. The 1L-WS_2 shows an emission peak near 2.0 eV corresponding to the direct interband recombination of the A exciton (*30*). An additional low-energy emission peak at 1.7 eV from the heterostructure is observed in addition to the emission of the A exciton of WS_2 and the singlet exciton of Tc. We have confirmed this low-energy emission peak in all the 1L-WS_2/Tc heterostructures fabricated. The intensity of the low-energy emission could vary significantly from sample to sample, probably due to the variations in morphology of different samples.

The 1L-WS_2 and the Tc molecules form a type II heterojunction, as schematically shown in Fig. 1C. The conduction band minimum (−3.4 eV) (*31*) of the 1L-WS_2 lies lower than the lowest unoccupied molecular orbital level (−2.4 eV) (*32*) of Tc molecules allowing electron transfer from Tc to WS_2, whereas the valence band maximum (VBM; −5.8 eV) (*31*) of WS_2 is located lower than the highest occupied molecular orbital (HOMO) level of Tc (−5.4 eV) (*32*), facilitating hole

Department of Chemistry, Purdue University, West Lafayette, IN 47907, USA.
*These authors contributed equally to this work.
†Corresponding author. Email: libai-huang@purdue.edu

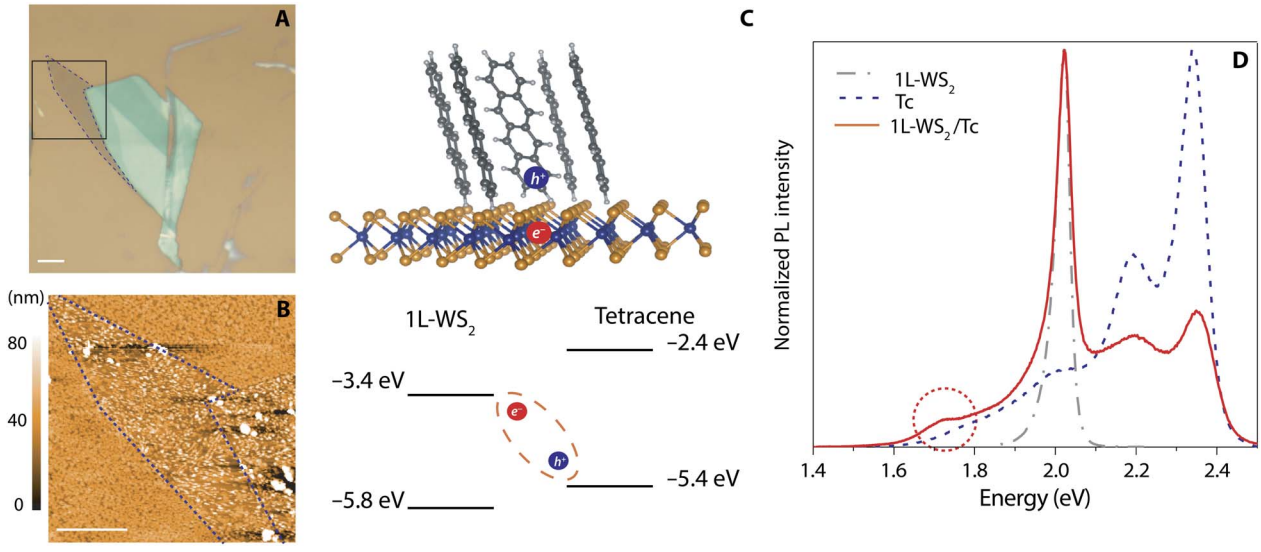

Fig. 1. Construction of a 1L-WS_2/Tc heterostructure. (**A**) Optical image of WS_2 flakes exfoliated on a Si/SiO_2 substrate. The 1L-WS_2 is indicated by the dashed line. The square shows the area imaged by AFM in (B). Scale bar, 10 μm. (**B**) AFM image of the same 1L-WS_2 flake in (A) with a Tc thin film deposited on top. Scale bar, 5 μm. (**C**) Schematic of the formation of CT excitons and the band alignment of the 1L-WS_2/Tc heterostructure, showing the formation of a type II heterojunction. (**D**) Steady-state PL spectra of a 1L-WS_2, Tc thin film, and a 1L-WS_2/Tc heterostructure. The new emission band at 1.7 eV indicates the formation of interlayer CT excitons.

transfer from WS_2 to Tc. On the basis of the band alignment, we attribute the emission band at 1.7 eV to interlayer CT excitons where the electrons and the holes reside on the 1L-WS_2 and the Tc film, respectively (Fig. 1C). We have also carried out PL excitation (PLE) measurements confirming the excitation of the A exciton in WS_2 leads to CT exciton emission (fig. S3). From the energy level alignment and 1.7-eV emission energy, the binding energy for the CT excitons is estimated to be ~0.3 eV, assuming that the energy levels do not change significantly at the interfaces. This binding energy is slightly larger than that of ~0.2 eV for the CT excitons in $MoSe_2$/WSe_2 heterostructures (*19*, *20*), which can be explained by the lower dielectric constant of the Tc thin film (ε ~ 5) in comparison to that for $MoSe_2$ (ε ~ 15) and WSe_2 (*4*), leading to less efficient screening of the Coulomb potential.

We monitor the CT exciton emission with a photoexcitation energy below the Tc bandgap at 2.1 eV exciting only WS_2 to eliminate the background emission from Tc at energy similar to the CT excitons. As shown in Fig. 2A, the emission from the interlayer CT excitons is broad, indicative of a distribution in CT exciton energy levels. The CT excitons exhibit overall much longer PL lifetime than the singlet exciton of the Tc (~100 ps) and the A exciton of WS_2 (~500 ps), as expected from the spatial indirect nature of the CT excitons (Fig. 2B). We have carried out excitation intensity–dependent measurements that show negligible variations in dynamics with fluences ranging from 1.25 to 125 μJ cm^{-2} (fig. S4), indicating that exciton-exciton annihilation processes do not play an important role here. The PL decay of the CT excitons is not a single exponential but only can be fitted with a stretched-exponential function

$$I(t) = I_0 e^{-\left(\frac{t}{\tau}\right)^{\beta}} \quad (1)$$

where τ = 0.97 ± 0.01 ns and β = 0.48 ± 0.01 is the stretching exponent (*33*). The need for a stretched-exponential fit is due to a superposition of many exponentials with different decay time constants τ_j (*33*, *34*) that probably arises from multiple configurations of the CT excitons. The dispersion of the decay time constant is described by β (0 < β < 1), where the smaller the β value, the broader the distribution of τ_j. The average exciton lifetime $\langle\tau_j\rangle$ is given as $\left(\frac{\tau}{\beta}\right)\Gamma\left(\frac{1}{\beta}\right) = 2.1$ ns, where Γ represents Gamma function (*34*). More discussion on different CT exciton states will be presented in the later part of the manuscript.

Hole transfer from WS_2 to Tc

We excite the 1L-WS_2/Tc heterostructure with a pump photon energy of 2.1 eV that is below the absorption edge of Tc (fig. S1) to selectively investigate hole transfer from WS_2 to Tc. The dynamics of the same 1L-WS_2 flake is probed at the A exciton bleach (2.0 eV) before and after Tc deposition (Fig. 2C). On the time scale of a few picoseconds, the dynamics become faster after the deposition of Tc, which can be explained by the additional hole-transfer pathway from WS_2 to Tc in the heterostructure. The dynamics before Tc deposition can be fitted with a biexponential decay function (Fig. 2C), and hole transfer is competing with the fast decay component on the picosecond time scale. We can extract the hole-transfer rate by subtracting the fast decay rate before Tc deposition from that of after Tc deposition and obtain a hole-transfer time constant of 3.2 ± 0.5 ps. This hole-transfer time is consistent with recent measurements at pentacene/MoS_2 interfaces (*15*).

To investigate driving force for dissociating the A exciton in WS_2, we perform measurements on WS_2/Tc heterostructures constructed with different thickness ranging from 1 layer to 7 layers (7L-WS_2) (fig. S5). The interlayer CT exciton emission disappears as the thickness of the WS_2 increases to two layers or thicker (Fig. 2A). There is also no obvious difference in the WS_2 transient absorption dynamics after Tc deposition (Fig. 2D for 2L-WS_2 and fig. S6 for 4L-WS_2, 5L-WS_2, and 7L-WS_2), implying that hole transfer does not occur, which explains the absence of the CT exciton in these heterostructures. This thickness dependence confirms that the below-bandgap emission is from CT excitons and not from defects or other origins.

In order for hole transfer to occur, the offset between the VBM of WS_2 and the HOMO of the Tc molecules that provides the driving force

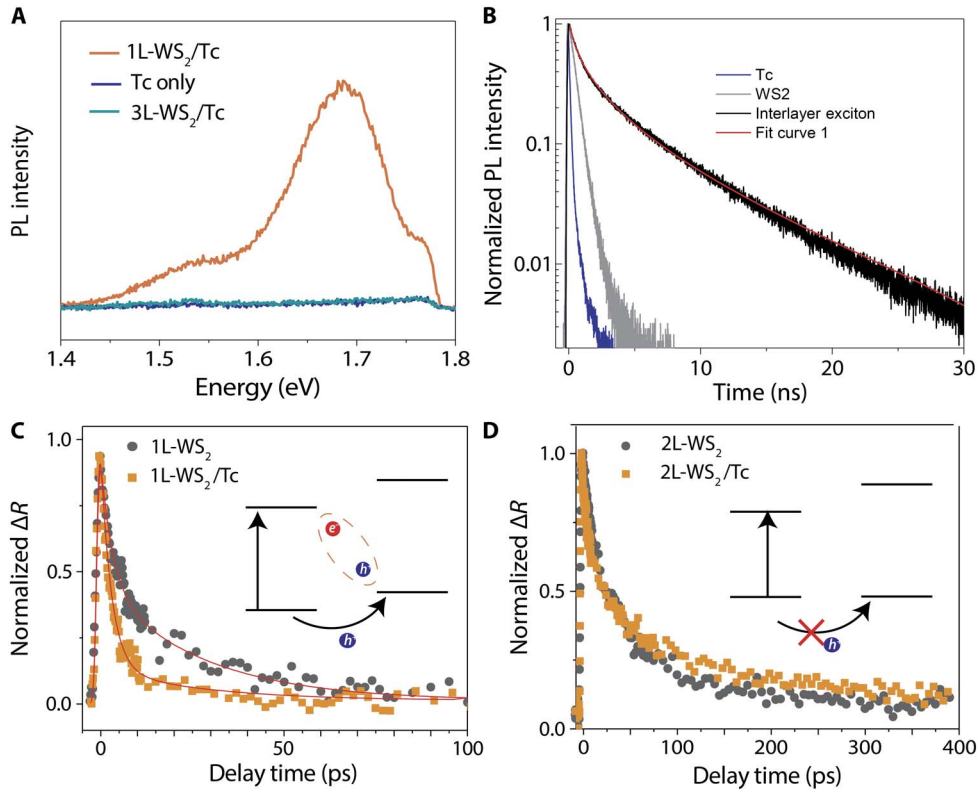

Fig. 2. Interlayer CT exciton emission and hole transfer from WS_2 to Tc. (**A**) PL spectra of a 1L-WS_2/Tc heterostructure, a 3L-WS_2/Tc heterostructure, and a Tc thin film with excitation energy of 2.1 eV and 700-nm long-pass filter selectively exciting WS_2 in the heterostructures and detecting only interlayer CT exciton emission. (**B**) Time-resolved PL measurements on the interlayer CT exciton in a 1L-WS_2/Tc heterostructure, a Tc film, and a 1L-WS_2 flake. The CT exciton PL decay is fitted with a stretched exponential function, as described in the main text. (**C**) Transient absorption dynamics probed at the A exciton bleach of the 1L-WS_2 before and after Tc deposition with a pump energy of 2.1 eV (pump fluence, 50 μJ cm^{-2}). Red solid lines are fittings with a biexponential function convoluted with an experimental response function. Inset: Band alignment shows the hole transfer process of the 1L-WS_2/Tc heterostructure. (**D**) Transient absorption dynamics probed at the A exciton bleach of 2L-WS_2 before and after Tc deposition with a pump energy of 2.1 eV, showing no hole transfer in the 2L-WS_2/Tc heterostructure.

(*35*) for A exciton dissociation has to be greater or similar to the A exciton binding energy of ~0.4 eV (*36*). This requirement is satisfied in 1L-WS_2/Tc heterostructures. However, as thickness increases to 2L-WS_2, the VBM energy level increases (*31*), and energy offset decreases to ~0.2 eV. The fact that hole transfer is not observed in the heterostructures constructed with 2L-WS_2 or thicker indicates that the energy offset between the VBM of WS_2 and the HOMO of Tc is not large enough to drive the dissociation of the A exciton in WS_2, and hence, the CT excitons do not form.

Electron versus energy transfer from Tc to WS_2

Next, we use a pump photon energy of 3.1 eV to investigate electron and energy transfer dynamics from Tc to WS_2. Under this condition, excitons are generated in both WS_2 and Tc. Because the singlet exciton emission of Tc overlaps with absorption spectrum of WS_2 (fig. S1), Förster-type resonance energy transfer from Tc to WS_2 is also possible. Dynamics probed at the A exciton resonance (2.0 eV) in WS_2 before and after Tc deposition are shown in Fig. 3 (A and B) for the 1L-WS_2/Tc and 2L-WS_2/Tc heterostructures, respectively. Note that measurements on Tc-only regions under the same experimental conditions show no detectable transient absorption signal when probing at 2.0 eV. Dynamics probed at the A exciton resonance become slower in the 1L-WS_2/Tc heterostructure than in the control 1L-WS_2 (Fig. 3A), which is the opposite from when only 1L-WS_2 is excited (Fig. 2C). The slower decay in the heterostructure could be due to either energy transfer or electron transfer from Tc to WS_2. We follow the procedure of Rowland *et al.* (*37*) to subtract the dynamics of the control 1L-WS_2 from that of the 1L-WS_2/Tc heterostructure (Fig. 3C), and a rise time of 2.1 ± 0.2 ps is obtained, which might contain contributions from both electron and energy transfer.

To separate the contribution from energy transfer, we examine dynamics in heterostructures constructed with 2L-WS_2 (Fig. 3B) and thicker (fig. S7). In these heterostructures, type I instead of type II heterojunctions are formed because hole transfer from WS_2 is blocked, and only exciton energy transfer is possible (schematically shown in Fig. 3D). After the deposition of Tc, the dynamics probed at the A exciton resonance become slower in these heterostructures when the Tc molecules are excited because of energy transfer. By subtracting the dynamics of the control 2L-WS_2 from that of the 2L-WS_2/Tc heterostructure, we obtain a rise time constant of 44 ± 5 ps corresponding to the energy transfer time from Tc to 2L-WS_2 (Fig. 3C). Energy transfer rates have been measured as a function of the thickness of WS_2, ranging from 2L to 7L, as plotted in Fig. 3E. Energy transfer rate decreases as the thickness of WS_2 increases, which is consistent with the recent reports on energy transfer between quantum dots and MoS_2 (*38*–*40*). This thickness dependence arises from the decreased electric field strength of the top layer WS_2 as thickness increases due to enhanced dielectric screening (*38*, *39*).

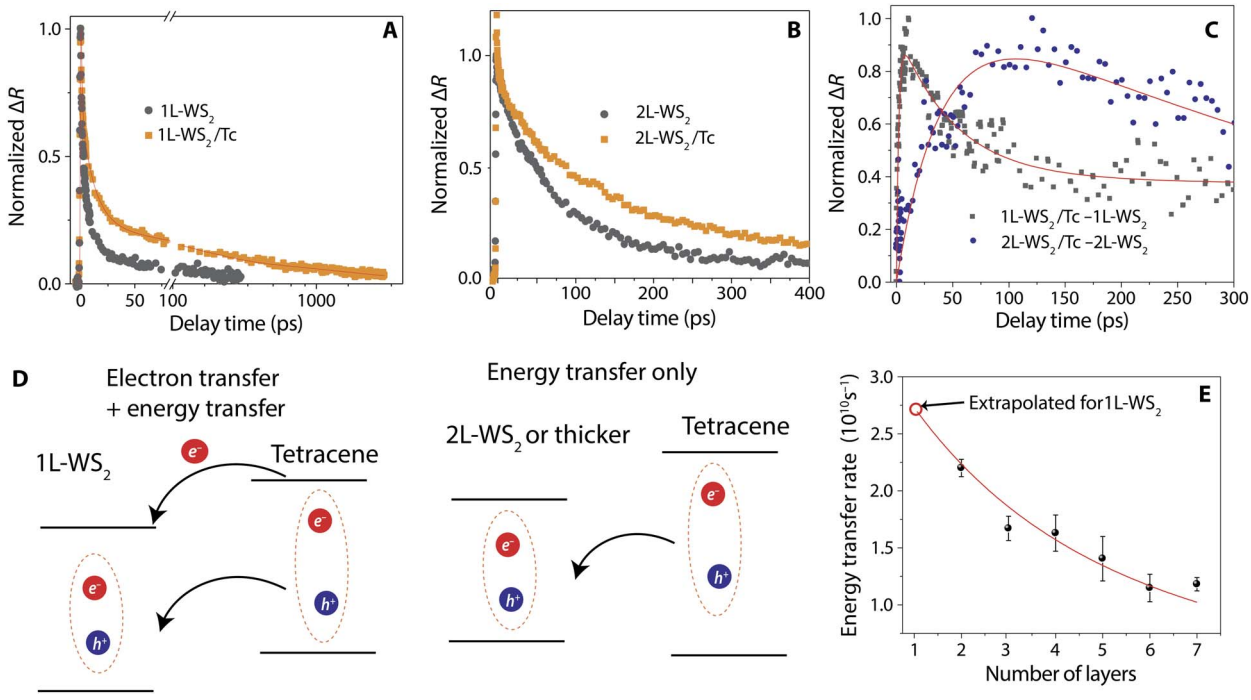

Fig. 3. Electron and energy transfer from Tc to WS_2. (**A**) 1L-WS_2 dynamics before and after Tc deposition. (**B**) 2L-WS_2 dynamics before and after Tc deposition. Pump = 3.1 eV (pump fluence, 2.2 μJ cm^{-2}) and probe = 2.0 eV. (**C**) Subtraction of 1L-WS_2 dynamics from 1L-WS_2/Tc dynamics fitted with a exponential growth function with a time constant of 2.1 ± 0.2 ps and subtraction of 2L-WS_2 dynamics from 2L-WS_2/Tc dynamics yielding a rise time constant of 44 ± 5 ps. (**D**) Schematic illustration of electron and energy transfer processes. In the heterostructures constructed from 2L-WS_2 or thicker, type I heterojunctions are formed, and only exciton energy transfer is possible. (**E**) Energy transfer rate dependence on numbers of WS_2 layers fitted to the electromagnetic model developed by Raja *et al.* (*39*), as described in the main text.

We fit the WS_2 thickness–dependent energy transfer rate by using the electromagnetic model developed by Raja *et al.* (*39*), as described in the Supplementary Notes, and by adopting 16.2 and 6.4 for the real and imaginary parts of dielectric constant for WS_2 (*41*), respectively. Using this model, a time constant of 37 ps is extrapolated for energy transfer from Tc to 1L-WS_2. Because this energy transfer time is more than one order of magnitude slower than the rise time of 2.1 ± 0.2 ps, we conclude that electron transfer instead of energy transfer dominates the dynamics in the 1L-WS_2/Tc heterostructure. The electron transfer time can be obtained by subtracting the energy transfer contribution from the rise time, $\frac{1}{\frac{1}{2.1\text{ ps}}-\frac{1}{37\text{ ps}}} = 2.2$ ps. Transient absorption dynamics of the 1L-WS_2/Tc heterostructure probed at the A exciton resonance show an additional slow decay with a characteristic time >1 ns (limited by the time window of the measurements), as shown in Fig. 3A, which is attributed to the recombination of the interlayer CT excitons.

Transport of the delocalized and localized CT excitons

A possible mechanism leading to the stretched-exponential behavior of the CT exciton PL decay as shown in Fig. 2B is trapping and detrapping dynamics between delocalized and localized states (*33*). This mechanism known as multiple trapping-detrapping has successfully explained the stretched-exponential PL decay observed in porous silicon (*42*). In WS_2/tetracene heterostructure, because CT exciton binding energy E_B is inversely proportional to the e-h distance, delocalized CT excitons with large e-h distance have smaller E_B and higher energy. When the e-h distance is reduced, the more localized CT excitons with lower energies can serve as traps (*43*). There could be certain sites to accommodate the lower-energy and more localized states where emission is more likely to occur (*25*). PL dynamics of the CT excitons are controlled by the competition between the diffusion to these sites and the detrapping of the exciton from these sites (*42*). The density and spatial distribution of the low-energy sites determine the dispersion of CT exciton lifetime and hence the value of β in Eq. 1 (*42*).

To validate the mechanism proposed, we image the transport of CT excitons directly with TAM by mapping population in both the spatial and temporal domains (*28*). The pump beam is held at a fixed position, whereas the probe beam is scanned relative to the pump with a pair of galvanometer scanners to obtain the exciton distribution at a given pump-probe delay time (more details in Materials and Methods and fig. S8). The pump-induced change in probe reflectance $\Delta R = R_{\text{pump - on}} - R_{\text{pump - off}}$ is collected. The pump energy is 3.1 eV exciting both WS_2 and Tc, and the probe energy is 2.0 eV probing WS_2. At zero delay time, the TAM results reflect the initial population created by the pump beam, and at later delay time, the TAM images directly visualize how excitons transport out of the initial volume. We have also carried out exciton transport experiments on a control 1L-WS_2 flake.

In 1D, the initial population $n(x,0)$ follows Gaussian distribution as created by a Gaussian pump beam of 3.1 eV at position (x_0) with a variance of σ_0^2 and is given by $n(x,0) = N\exp\left[-\frac{(x-x_0)^2}{2\sigma_0^2}\right]$. Population as a function of space and time can be described by a differential equation that includes both the diffusion out of the initial volume and population decay, which is given by

$$\frac{\partial n(x,t)}{\partial t} = D\frac{\partial^2 n(x,t)}{\partial x^2} - \frac{n(x,t)}{\tau} \quad (2)$$

where D is the exciton diffusion constant and τ is the exciton lifetime. Solution to Eq. 2 dictates that exciton distribution at any later delay time (t) is also Gaussian and can be described as $n(x,t) = N\exp\left[-\frac{(x-x_0)^2}{2\sigma_t^2}\right]$ with a variance of σ_t^2. The solution also gives the diffusion constant D as

$$D = \frac{\sigma_t^2 - \sigma_0^2}{2t} \quad (3)$$

Using this analysis, the population of the A excitons in the control 1L-WS_2 flake is fitted to Gaussian functions at different delay times, and the diffusion constant is determined to be 1.7 ± 0.1 $cm^2\ s^{-1}$ (Fig. 4, A and B).

For the 1L-WS_2/Tc heterostructure, population profiles at different delay times have been taken along the line indicated in Fig. 4C with a pump fluence of 4.4 μJ cm^{-2}. Sums of at least two Gaussian functions are required to fit the population profile at a given pump-probe delay time (Fig. 4D and fig. S9), as given by $n(x,t) = N_1\exp\left[-\frac{(x-x_0)^2}{2\sigma_{1,t}^2}\right] + N_2\exp\left[-\frac{(x-x_0)^2}{2\sigma_{2,t}^2}\right]$, implying that there are at least two populations migrating with different diffusion constants. The extracted $\sigma_{1,t}^2$ and $\sigma_{2,t}^2$ are plotted as a function of pump-probe delay time in Fig. 4E. Very rapid diffusion is observed before 100 ps, possibly due to the transport of the free electrons in the 1L-WS_2 dissociated from the hot CT exciton states created by the 3.1-eV pump that has 1.4-eV excess energy (*1*).

We focus on time scales > 100 ps where the intralayer A excitons in the 1L-WS_2 have mostly decayed (Fig. 3A). The long-lived transient absorption signal in the heterostructures reflects the CT exciton population because the formation of CT excitons leaves the electronic states occupied in WS_2 and results in the long-lived bleaching of A exciton transition. A diffusion constant D_1 = 1.0 ± 0.1 $cm^2\ s^{-1}$ is obtained in the heterostructure for delay time > 100 ps by fitting the time dependence of σ_1^2, corresponding to the fast-moving population with N_1 = 0.4. The diffusion constant for the slow moving population (N_2 = 0.6) is more than one order of magnitude slower, D_2 = 0.04 ± 0.01 $cm^2\ s^{-1}$.

To correctly measure exciton transport, it is important to account for exciton-exciton annihilation processes. Because the exciton density at the center of the spot is higher than at the edge, exciton-exciton annihilation could lead to artificially broadening of σ. We have carried out pump intensity–dependent dynamics and transport measurements to rule out the interference from exciton-exciton annihilation. Transient absorption dynamics measured at pump fluences from 2.2 to 20.6 μJ cm^{-2} exhibit essentially the same decay (fig. S10). TAM measurements at two higher pump fluences of 10.0 and 20.6 μJ cm^{-2} show a similar bipopulation diffusion behavior (figs. S11 and S12). These measurements yield almost identical diffusion constants as those measured at 4.4 μJ cm^{-2},

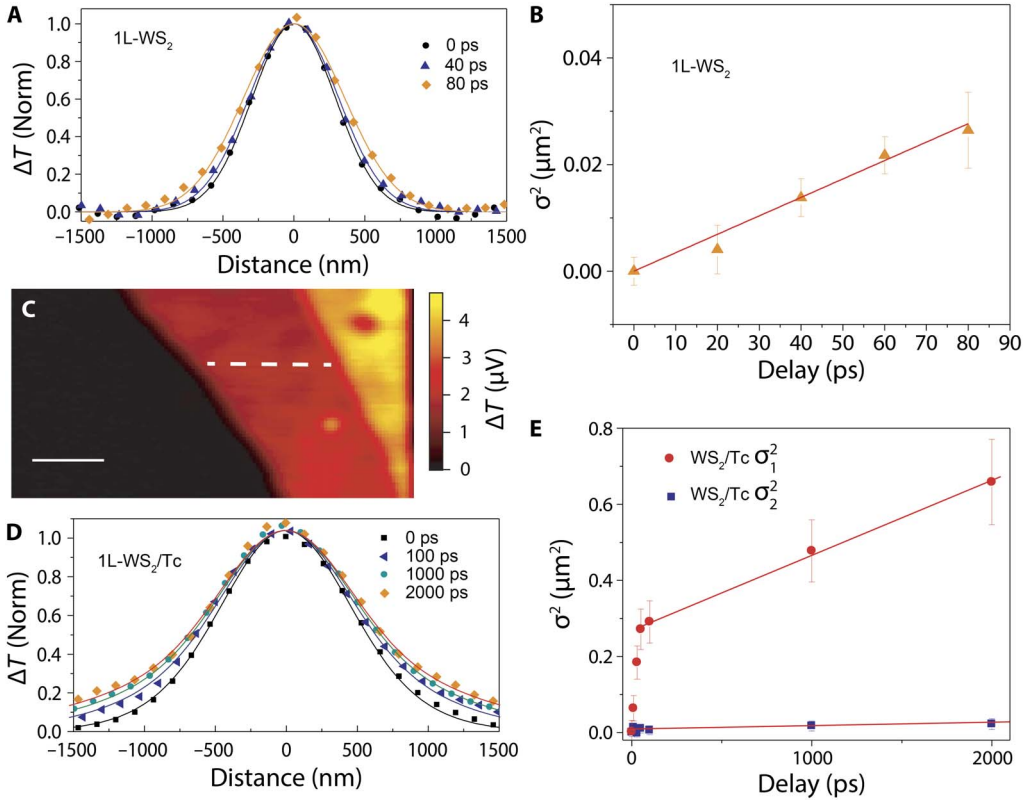

Fig. 4. Transport of interlayer CT excitons. (**A**) Exciton population profiles fitted with Gaussian functions at different delay times with the maximum Δ*T* signal normalized (Norm) to unity for the control 1L-WS_2. The pump photon energy is 3.1 eV (pump fluence, 4.4 μJ cm^{-2}), and the probe energy is 2.0 eV. (**B**) $\sigma_t^2 - \sigma_0^2$ as a function of pump-probe delay time, with a linear fit to Eq. 3 (line) for the control 1L-WS_2. Error bars of $\sigma_t^2 - \sigma_0^2$ are the SEs estimated from Gaussian fitting to the spatial intensity distributions. (**C**) TAM image of the same 1L-WS_2/Tc heterostructure shown in Fig. 1 taken with spatially overlapped pump and probe beams at 0 ps. Scale bar, 2 μm. The pump energy is 3.1 eV (pump fluence, 4.4 μJ cm^{-2}), and the probe energy is 2.0 eV. (**D**) Exciton population profiles fitted with a sum of two Gaussian functions as described in the text at different delay times with the maximum Δ*R* signal normalized to unity for the 1L-WS_2/Tc heterostructure along the line indicated in (C). (**E**) $\sigma_{1,t}^2 - \sigma_0^2$ and $\sigma_{2,t}^2 - \sigma_0^2$ as a function of pump-probe delay time, with a linear fit to Eq. 3 (line) for the 1L-WS_2/Tc heterostructure.

with $D_1 = 1.0 \pm 0.1$ cm^2 s^{-1} and $D_2 = 0.04 \pm 0.01$ cm^2 s^{-1} for pump fluence at 10.0 μJ cm^{-2} (fig. S11) and $D_1 = 0.9 \pm 0.1$ cm^2 s^{-1} and $D_2 = 0.03 \pm 0.02$ cm^2 s^{-1} for pump fluence at 20.6 μJ cm^{-2} (fig. S12), respectively. The lack of pump intensity dependence implies that exciton-exciton annihilation processes do not contribute to the two diffusion constants measured. It has been established that the exciton-exciton annihilation threshold in single-layer TMDCs is as low as nanojoule per squared centimeter (*44*). However, the key difference in the 1L-WS_2/Tc heterostructures is that charge transfer processes occur at 2- to 3-ps time scales, much shorter than exciton-exciton annihilation time of hundreds of picoseconds in monolayer WS_2 (*45*). Therefore, formation of CT excitons outcompetes exciton-exciton annihilation, leading to a much less pronounced annihilation.

The fact that there exist at least two CT exciton populations with different diffusion constants directly supports the delocalized and localized states proposed to explain the stretched-exponential PL decay behavior. We attribute the fast-moving population to the CT excitons with a large e-h distance. It is likely that the fast-moving population also leads to the dissociated free electrons. The slow-moving population is the more localized CT excitons trapped at low-energy sites. The energy difference Δ between the delocalized and localized states can be estimated by $\frac{N1}{N2} = e^{-\frac{\Delta}{k_B T}}$, where k_B is the Boltzmann constant and T is temperature. Δ has a value of ~10 meV < $k_B T$ at room temperature, allowing for detrapping of exciton from the localized states and resulting in the stretched-exponential decay behavior.

A diffusion constant as high as 1 cm^2 s^{-1} for CT excitons is remarkable, which indicates that the diffusion length, $L = \sqrt{D\tau}$, is up to ~450 nm when using an average lifetime of 2 ns. A possible explanation for the extremely mobile CT excitons is that the electron mobility in WS_2 of ~50 cm^2 s^{-1} V^{-1} (*46*) is more than one order of magnitude higher than the hole mobility in Tc (~1 cm^2 s^{-1} V^{-1}) (*47*). CT exciton transport has been proposed to occur via asynchronous electron and hole motion (*25*). Because the mobile electrons in the WS_2 layer can sample a much larger distance than the holes in Tc, large e-h distances can be achieved (*35*). Dimensionality could also play an important role in increasing e-h distances as suggested by recent theoretical simulations where 2D electron transport increases the dissociation yield of CT excitons by an order of magnitude over 1D case (*27*). CT exciton mobility of ~10 cm^2 s^{-1} has also been reported in $MoSe_2$/WSe_2 interfaces (*17*).

The highly mobile CT excitons at the crystalline 2D organic-inorganic interfaces can lead to large e-h distances and facilitate exciton dissociation at interfaces, which could have important implications for charge separation in excitonic solar cells. For instance, the interfaces between conjugated polymer donors and fullerene acceptors are highly crystalline at the length scale of a few nanometers in organic solar cells, despite the system being highly disordered overall (*5*). The mobile CT excitons at the crystalline nanoscale interfaces could sample large distances in a short time (10 nm in 1 ps assuming $D = 1$ cm^2 s^{-1}), which could be the key factor for overcoming large CT exciton binding energy to achieve efficient charge separation.

CONCLUSION

In conclusion, the formation and transport of interlayer CT excitons have been elucidated in 2D organic-inorganic vdW heterostructures constructed from WS_2 layers and tetracene thin films. PL measurements confirm the formation of interlayer excitons with a binding energy of ~0.3 eV. Electron- and hole-transfer processes at the interface between monolayer WS_2 and tetracene thin film are very rapid, with time constants of ~2 and ~3 ps, respectively. TAM measurements of exciton transport at these 2D interfaces reveal coexistence of delocalized and localized CT excitons, with diffusion constants of ~1 cm^2 s^{-1} and ~0.04 cm^2 s^{-1}, respectively. The trapping-detrapping dynamics of the delocalized and localized states leads to stretch-exponential PL decay. The high mobility of the delocalized CT excitons could be the key factor to overcome large CT exciton binding energy in achieving efficient charge separation.

MATERIALS AND METHODS

Sample preparations

WS_2 flakes of different thicknesses were obtained by mechanically exfoliating bulk WS_2 onto Si/SiO_2 substrates. WS_2 flakes from one to seven layers have been exfoliated and integrated with Tc thin film to fabricate the heterostructures. The number of WS_2 layers was identified by PL microscopy (Supplementary Notes). Tetracene thin film was deposited onto WS_2 flakes by the physical vapor deposition method (Supplementary Notes). The Tc film thickness of ~20 nm was measured by AFM measurements.

Steady-state and time-resolved PL

Steady-state and time-resolved PL measurements have been performed by a home-built confocal micro-PL setup. A picosecond-pulsed diode laser (LDH-P-C-450B, PicoQuant) with and excitation energy of 2.8 eV (full width at half maximum, 50 ps) was used to excite the sample, which was focused by a 50× [numerical aperture (NA), 0.95] objective. The beam size in PL measurements was ~1 μm, smaller than our sample size. The PL emission was collected with the same objective, dispersed with a monochromator (Andor Technology), and detected by a thermoelectric-cooled charge-coupled device (Andor Technology). Time-resolved PL was measured using a single-photon avalanche diode (PDM series, PicoQuant) and a single-photon counting module (PicoQuant). The time resolution of the time-resolved PL setup is ~100 ps. Measurements with excitation energy of 2.1 eV were carried out with an optical parametric amplifier (OPA; TOPAS-Twins, Light Conversion Ltd) pumped by a high-repetition rate amplifier (400 KHz, PHAROS, Light Conversion Ltd.).

Transient absorption dynamics

Two independent OPAs (TOPAS-Twins, Light Conversion Ltd.) pumped by the output of a high-repetition rate amplifier (400 KHz, PHAROS, Light Conversion Ltd.) provided the pump and probe beams. One OPA provided the pump, and the other supplied the probe. An acousto-optic modulator (R23080-1, Gooch and Housego) was used to modulate the pump beam at 100 kHz. A mechanical translation stage (DDS600-E, Thorlabs) was used to delay the probe with respect to the pump. Both the pump and probe beams were spatially filtered before being focused onto the sample by a 40× (NA, 0.60) objective (CFI Apo TIRF, Nikon Inc.) The probe beam was collected by the same objective and was detected by an avalanche photodiode (APD) (C5331-04, Hamamatsu). The change in the probe reflectance (ΔR) induced by the pump was detected by a lock-in amplifier.

Transient absorption microscopy

A Ti:sapphire oscillator (Coherent Mira 900) pumped by a Verdi diode laser (Coherent Verdi V18) was used as the light source (output at 1.6 eV, 80-MHz repetition rate). Seventy percent of the pulse energy was fed into the optical parametric oscillator (Coherent Mira OPO) to generate probe light at 2.0 eV, whereas the remaining 30% was

doubled to 3.1 eV and served as the pump beam. The repetition rate of both beams was reduced to 2.5 MHz using two clock-synchronized pulse pickers (Model 9200, Coherent Inc.). The pump beam was modulated at 1 MHz using an acoustic optical modulator (R21080-1DM, Gooch and Housego). A 40× (NA, 0.60) objective (CFI Apo TIRF, Nikon Inc.) was used to focus the laser beams onto the sample, and the reflection light was collected by the same objective and detected by an APD (C5331-04, Hamamatsu). A galvanometer scanner (GVS012, Thorlabs) was used to scan the probe beam relative to the pump beam in space to obtain the exciton diffusion profiles. A schematic of the TAM setup is presented in fig. S8.

SUPPLEMENTARY MATERIALS

Supplementary material for this article is available at http://advances.sciencemag.org/cgi/content/full/4/1/eaao3104/DC1

Supplementary Notes
section S1. Physical vapor deposition of tetracene
section S2. AFM
section S3. Microreflection microscopy
section S4. Factors that limits the spatial precision of TAM imaging
section S5. Thickness-dependent energy transfer from Tc to WS_2
fig. S1. Absorption and PL spectrum of Tc film and 1L-WS_2.
fig. S2. AFM line profile of the Tc film thickness.
fig. S3. PLE measurements.
fig. S4. Excitation intensity–dependent measurements of PL dynamics of CT exciton emission.
fig. S5. Identification of numbers of WS_2 layers using PL spectroscopy.
fig. S6. TAM dynamics of 4L to 7L WS_2 before and after Tc deposition.
fig. S7. Energy transfer from Tc to WS_2 measured with TAM (3.1-eV pump and 2.0-eV probe).
fig. S8. Schematics of the TAM setup.
fig. S9. CT exciton population profile fitted with a single Gaussian function and a sum of two Gaussian functions.
fig. S10. Transient absorption dynamics of a 1L-WS_2/Tc heterostructure measured at different pump fluences.
fig. S11. TAM of CT exciton diffusion measured at 10.0 μJ cm^{-2}.
fig. S12. TAM of CT exciton diffusion measured at 20.6 μJ cm^{-2}.

REFERENCES AND NOTES

1. A. E. Jailaubekov, A. P. Willard, J. R. Tritsch, W.-L. Chan, N. Sai, R. Gearba, L. G. Kaake, K. J. Williams, K. Leung, P. J. Rossky, X.-Y. Zhu, Hot charge-transfer excitons set the time limit for charge separation at donor/acceptor interfaces in organic photovoltaics. *Nat. Mater.* **12**, 66–73 (2013).
2. K. Vandewal, S. Albrecht, E. T. Hoke, K. R. Graham, J. Widmer, J. D. Douglas, M. Schubert, W. R. Mateker, J. T. Bloking, G. F. Burkhard, A. Sellinger, J. M. J. Fréchet, A. Amassian, M. K. Riede, M. D. McGehee, D. Neher, A. Salleo, Efficient charge generation by relaxed charge-transfer states at organic interfaces. *Nat. Mater.* **13**, 63–68 (2014).
3. S. M. Falke, C. A. Rozzi, D. Brida, M. Maiuri, M. Amato, E. Sommer, A. De Sio, A. Rubio, G. Cerullo, E. Molinari, C. Lienau, Coherent ultrafast charge transfer in an organic photovoltaic blend. *Science* **344**, 1001–1005 (2014).
4. X. Zhu, N. R. Monahan, Z. Gong, H. Zhu, K. W. Williams, C. A. Nelson, Charge transfer excitons at van der Waals interfaces. *J. Am. Chem. Soc.* **137**, 8313–8320 (2015).
5. A. C. Jakowetz, M. L. Böhm, A. Sadhanala, S. Huettner, A. Rao, R. H. Friend, Visualizing excitations at buried heterojunctions in organic semiconductor blends. *Nat. Mater.* **16**, 551–557 (2017).
6. L. Britnell, R. V. Gorbachev, R. Jalil, B. D. Belle, F. Schedin, A. Mishchenko, T. Georgiou, M. I. Katsnelson, L. Eaves, S. V. Morozov, N. M. R. Peres, J. Leist, A. K. Geim, K. S. Novoselov, L. A. Ponomarenko, Field-effect tunneling transistor based on vertical graphene heterostructures. *Science* **335**, 947–950 (2012).
7. T. Georgiou, R. Jalil, B. D. Belle, L. Britnell, R. V. Gorbachev, S. V. Morozov, Y.-J. Kim, A. Gholinia, S. J. Haigh, O. Makarovsky, L. Eaves, L. A. Ponomarenko, A. K. Geim, K. S. Novoselov, A. Mishchenko, Vertical field-effect transistor based on graphene–WS_2 heterostructures for flexible and transparent electronics. *Nat. Nanotechnol.* **8**, 100–103 (2013).
8. A. Mishchenko, J. S. Tu, Y. Cao, R. V. Gorbachev, J. R. Wallbank, M. T. Greenaway, V. E. Morozov, S. V. Morozov, M. J. Zhu, S. L. Wong, F. Withers, C. R. Woods, Y.-J. Kim, K. Watanabe, T. Taniguchi, E. E. Vdovin, O. Makarovsky, T. M. Fromhold, V. I. Fal'ko, A. K. Geim, L. Eaves, K. S. Novoselov, Twist-controlled resonant tunnelling in graphene/boron nitride/graphene heterostructures. *Nat. Nanotechnol.* **9**, 808–813 (2014).
9. W. J. Yu, Y. Liu, H. Zhou, A. Yin, Z. Li, Y. Huang, X. Duan, Highly efficient gate-tunable photocurrent generation in vertical heterostructures of layered materials. *Nat. Nanotechnol.* **8**, 952–958 (2013).
10. A. K. Geim, I. V. Grigorieva, Van der Waals heterostructures. *Nature* **499**, 419–425 (2013).
11. E. H. Cho, W. G. Song, C. J. Park, J. Kim, S. Kim, J. Joo, Enhancement of photoresponsive electrical characteristics of multilayer MoS_2 transistors using rubrene patches. *Nano Res.* **8**, 790–800 (2015).
12. D. Jariwala, T. J. Marks, M. C. Hersam, Mixed-dimensional van der Waals heterostructures. *Nat. Mater.* **16**, 170–181 (2017).
13. D. Jariwala, S. L. Howell, K.-S. Chen, J. Kang, V. K. Sangwan, S. A. Filippone, R. Turrisi, T. J. Marks, L. J. Lauhon, M. C. Hersam, Hybrid, gate-tunable, van der Waals p–n heterojunctions from pentacene and MoS_2. *Nano Lett.* **16**, 497–503 (2016).
14. X. Liu, J. Gu, K. Ding, D. Fan, X. Hu, Y.-W. Tseng, Y.-H. Lee, V. Menon, S. R. Forrest, Photoresponse of an organic semiconductor/two-dimensional transition metal dichalcogenide heterojunction. *Nano Lett.* **17**, 3176–3181 (2017).
15. S. Bettis Homan, V. K. Sangwan, I. Balla, H. Bergeron, E. A. Weiss, M. C. Hersam, Ultrafast exciton dissociation and long-lived charge separation in a photovoltaic pentacene–MoS_2 van der Waals heterojunction. *Nano Lett.* **17**, 164–169 (2017).
16. H. Fang, C. Battaglia, C. Carraro, S. Nemsak, B. Ozdol, J. S. Kang, H. A. Bechtel, S. B. Desai, F. Kronast, A. A. Unal, G. Conti, C. Conlon, G. K. Palsson, M. C. Martin, A. M. Minor, C. S. Fadley, E. Yablonovitch, R. Maboudian, A. Javey, Strong interlayer coupling in van der Waals heterostructures built from single-layer chalcogenides. *Proc. Natl. Acad. Sci.* **111**, 6198–6202 (2014).
17. F. Ceballos, M. Z. Bellus, H.-Y. Chiu, H. Zhao, Probing charge transfer excitons in a $MoSe_2$–WS_2 van der Waals heterostructure. *Nanoscale* **7**, 17523–17528 (2015).
18. X. Hong, J. Kim, S.-F. Shi, Y. Zhang, C. Jin, Y. Sun, S. Tongay, J. Wu, Y. Zhang, F. Wang, Ultrafast charge transfer in atomically thin MoS_2/WS_2 heterostructures. *Nat. Nanotechnol.* **9**, 682–686 (2014).
19. H. Zhu, J. Wang, Z. Gong, Y. D. Kim, J. Hone, X.-Y. Zhu, Interfacial charge transfer circumventing momentum mismatch at two-dimensional van der Waals heterojunctions. *Nano Lett.* **17**, 3591–3598 (2017).
20. N. R. Wilson, P. V. Nguyen, K. Seyler, P. Rivera, A. J. Marsden, Z. P. L. Laker, G. C. Constantinescu, V. Kandyba, A. Barinov, N. D. M. Hine, X. Xu, D. H. Cobden, Determination of band offsets, hybridization, and exciton binding in 2D semiconductor heterostructures. *Sci. Adv.* **3**, e1601832 (2017).
21. H. Heo, J. H. Sung, S. Cha, B.-G. Jang, J.-Y. Kim, G. Jin, D. Lee, J.-H. Ahn, M.-J. Lee, J. H. Shim, H. Choi, M.-H. Jo, Interlayer orientation-dependent light absorption and emission in monolayer semiconductor stacks. *Nat. Commun.* **6**, 7372 (2015).
22. P. K. Nayak, Y. Horbatenko, S. Ahn, G. Kim, J.-U. Lee, K. Y. Ma, A.-R. Jang, H. Lim, D. Kim, S. Ryu, H. Cheong, N. Park, H. S. Shin, Probing evolution of twist-angle-dependent interlayer excitons in $MoSe_2$/WSe_2 van der Waals heterostructures. *ACS Nano* **11**, 4041–4050 (2017).
23. P. Rivera, J. R. Schaibley, A. M. Jones, J. S. Ross, S. Wu, G. Aivazian, P. Klement, K. Seyler, G. Clark, N. J. Ghimire, J. Yan, D. G. Mandrus, W. Yao, X. Xu, Observation of long-lived interlayer excitons in monolayer $MoSe_2$–WSe_2 heterostructures. *Nat. Commun.* **6**, 6242 (2015).
24. P. Rivera, K. L. Seyler, H. Yu, J. R. Schaibley, J. Yan, D. G. Mandrus, W. Yao, X. Xu, Valley-polarized exciton dynamics in a 2D semiconductor heterostructure. *Science* **351**, 688–691 (2016).
25. P. B. Deotare, W. Chang, E. Hontz, D. N. Congreve, L. Shi, P. D. Reusswig, B. Modtland, M. E. Bahlke, C. K. Lee, A. P. Willard, V. Bulović, T. Van Voorhis, M. A. Baldo, Nanoscale transport of charge-transfer states in organic donor–acceptor blends. *Nat. Mater.* **14**, 1130–1134 (2015).
26. B. Bernardo, D. Cheyns, B. Verreet, R. D. Schaller, B. P. Rand, N. C. Giebink, Delocalization and dielectric screening of charge transfer states in organic photovoltaic cells. *Nat. Commun.* **5**, 3245 (2014).
27. S. Athanasopoulos, S. Tscheuschner, H. Bässler, A. Köhler, Efficient charge separation of cold charge-transfer states in organic solar cells through incoherent hopping. *J. Phys. Chem. Lett.* **2017**, 2093–2098 (2017).
28. Y. Wan, Z. Guo, T. Zhu, S. Yan, J. Johnson, L. Huang, Cooperative singlet and triplet exciton transport in tetracene crystals visualized by ultrafast microscopy. *Nat. Chem.* **7**, 785–792 (2015).
29. C.-H. Lee, T. Schiros, E. J. G. Santos, B. Kim, K. G. Yager, S. J. Kang, S. Lee, J. Yu, K. Watanabe, T. Taniguchi, J. Hone, E. Kaxiras, C. Nuckolls, P. Kim, Epitaxial growth of molecular crystals on van der Waals substrates for high-performance organic electronics. *Adv. Mater.* **26**, 2812–2817 (2014).
30. W. Zhao, Z. Ghorannevis, L. Chu, M. Toh, C. Kloc, P.-H. Tan, G. Eda, Evolution of electronic structure in atomically thin sheets of WS_2 and WSe_2. *ACS Nano* **7**, 791–797 (2013).
31. H. Zeng, G.-B. Liu, J. Dai, Y. Yan, B. Zhu, R. He, L. Xie, S. Xu, X. Chen, W. Yao, X. Cui, Optical signature of symmetry variations and spin-valley coupling in atomically thin tungsten dichalcogenides. *Sci. Rep.* **3**, 1608 (2013).

32. P. Hu, H. Li, Y. Li, H. Jiang, C. Kloc, Single-crystal growth, structures, charge transfer and transport properties of anthracene-F_4TCNQ and tetracene-F_4TCNQ charge-transfer compounds. *CrstEngComm* **19**, 618–624 (2017).
33. R. Chen, Apparent stretched-exponential luminescence decay in crystalline solids. *JOL* **102–103**, 510–518 (2003).
34. S. Lu, A. Madhukar, Nonradiative resonant excitation transfer from nanocrystal quantum dots to adjacent quantum channels. *Nano Lett.* **7**, 3443–3451 (2007).
35. P. Peumans, S. R. Forrest, Separation of geminate charge-pairs at donor–acceptor interfaces in disordered solids. *Chem. Phys. Lett.* **398**, 27–31 (2004).
36. A. Chernikov, T. C. Berkelbach, H. M. Hill, A. Rigosi, Y. Li, O. B. Aslan, D. R. Reichman, M. S. Hybertsen, T. F. Heinz, Exciton binding energy and nonhydrogenic Rydberg series in monolayer WS_2. *Phys. Rev. Lett.* **113**, 076802 (2014).
37. C. E. Rowland, I. Fedin, H. Zhang, S. K. Gray, A. O. Govorov, D. V. Talapin, R. D. Schaller, Picosecond energy transfer and multiexciton transfer outpaces Auger recombination in binary CdSe nanoplatelet solids. *Nat. Mater.* **14**, 484–489 (2015).
38. F. Prins, A. J. Goodman, W. A. Tisdale, Reduced dielectric screening and enhanced energy transfer in single-and few-layer MoS_2. *Nano Lett.* **14**, 6087–6091 (2014).
39. A. Raja, A. Montoya-Castillo, J. Zultak, X.-X. Zhang, Z. Ye, C. Roquelet, D. A. Chenet, A. M. van der Zande, P. Huang, S. Jockusch, J. Hone, D. R. Reichman, L. E. Brus, T. F. Heinz, Energy transfer from quantum dots to graphene and MoS_2: The role of absorption and screening in two-dimensional materials. *Nano Lett.* **16**, 2328–2333 (2016).
40. H. Zang, P. K. Routh, Y. Huang, J.-S. Chen, E. Sutter, P. Sutter, M. Cotlet, Nonradiative energy transfer from individual CdSe/ZnS quantum dots to single-layer and few-layer tin disulfide. *ACS Nano* **10**, 4790–4796 (2016).
41. Y. Li, A. Chernikov, X. Zhang, A. Rigosi, H. M. Hill, A. M. van der Zande, D. A. Chenet, E.-M. Shih, J. Hone, T. F. Heinz, Measurement of the optical dielectric function of monolayer transition-metal dichalcogenides: MoS_2, $MoSe_2$, WS_2, and WSe_2. *Phys. Rev. B* **90**, 205422 (2014).
42. L. Pavesi, M. Ceschini, Stretched-exponential decay of the luminescence in porous silicon. *Phys. Rev. B* **48**, 17625–17628 (1993).
43. C. K. Lee, L. Shi, A. P. Willard, A model of charge-transfer excitons: Diffusion, spin dynamics, and magnetic field effects. *J. Phys. Chem. Lett.* **7**, 2246–2251 (2016).
44. M. Amani, D.-H. Lien, D. Kiriya, J. Xiao, A. Azcatl, J. Noh, S. R. Madhvapathy, R. Addou, S. KC, M. Dubey, K. Cho, R. M. Wallace, S.-C. Lee, J.-H. He, J. W. Ager III, X. Zhang, E. Yablonovitch, A. Javey, Near-unity photoluminescence quantum yield in MoS_2. *Science* **350**, 1065–1068 (2015).
45. L. Yuan, L. Huang, Exciton dynamics and annihilation in WS_2 2D semiconductors. *Nanoscale* **7**, 7402–7408 (2015).
46. D. Ovchinnikov, A. Allain, Y.-S. Huang, D. Dumcenco, A. Kis, Electrical transport properties of single-layer WS_2. *ACS Nano* **8**, 8174–8181 (2014).
47. J. Berrehar, P. Delannoy, M. Schotta, Drift mobility of holes in crystalline tetracene. *Phys. Status Solidi B Basic Solid State Phys.* **77**, K119–K122 (1976).

Acknowledgments

Funding: L.H., T.Z, and L.Y. acknowledge the support from U.S. Department of Energy, Office of Basic Energy Sciences through award DE-SC0016356. Y.Z. and J.M. appreciate the financial support from the Office of Naval Research Young Investigator Program, award number N00014-16-1-2551 (program manager: P. Armistead). **Author contributions:** L.H., T.Z., and L.Y. designed the experiments. T.Z. and L.Y. carried out the optical measurements. Y.Z. and J.M. contributed to materials growth and characterization. M.Z. contributed sample preparations. Y.W. contributed to instrumental developments. L.H., T.Z., and L.Y. analyzed and modeled the data. L.H., T.Z., and L.Y. wrote the manuscript with inputs from all authors. **Competing interests:** The authors declare that they have no competing interests. **Data and materials availability:** All data needed to evaluate the conclusions in the paper are present in the paper and/or the Supplementary Materials. Additional data related to this paper may be requested from the authors.

Submitted 6 July 2017
Accepted 1 December 2017
Published 12 January 2018
10.1126/sciadv.aao3104

Citation: T. Zhu, L. Yuan, Y. Zhao, M. Zhou, Y. Wan, J. Mei, L. Huang, Highly mobile charge-transfer excitons in two-dimensional WS_2/tetracene heterostructures. *Sci. Adv.* **4**, eaao3104 (2018).

Science Advances

Highly mobile charge-transfer excitons in two-dimensional WS_2/tetracene heterostructures

Tong Zhu, Long Yuan, Yan Zhao, Mingwei Zhou, Yan Wan, Jianguo Mei and Libai Huang

Sci Adv **4** (1), eaao3104.
DOI: 10.1126/sciadv.aao3104